# ORBIT AND ATTITUDE PERTURBATIONS DUE TO AERODYNAMICS AND RADIATION PRESSURE

H. Klinkrad[1] and B. Fritsche[2]

[1]Mission Analysis Section, ESA/ESOC, D-64293 Darmstadt, Germany
[2]Hypersonic Technology Göttingen, D-37191 Katlenburg-Lindau, Germany

ABSTRACT

For satellites which are operated in low-Earth orbits (LEO), gravitational forces due to the non-uniform mass distribution of the Earth are dominating the orbit and attitude perturbation spectra. Non-gravitational forces are mainly caused by momentum exchange with the spacecraft surface, and they are mostly of second order. The most prominent of these forces originate from the interaction of the spacecraft surface with molecules and ions of the thermosphere, and from the impact of photons which come directly from the sun, which are reflected as albedo from the illuminated Earth hemisphere, or which are re-emitted by the whole Earth as delayed infra-red (IR) re-radiation. In contrast with gravitational perturbations, the aerodynamic and radiation pressure effects are difficult to model since they require a good knowledge of the spacecraft geometry and surface properties, and they also require reliable estimates of the molecule and photon particle flux. The necessary models of the thermosphere, and of the Earth albedo and IR re-radiation distributions are depending on a large set of parameters, including the spacecraft location, the time, the season (sun position), and solar and geomagnetic activity levels. The variability of these environment models will be explained, and mathematical models will be described which allow to use the resulting molecule and photon flux models to compute perturbing forces and torques acting on a LEO satellite. Examples will be provided for ESA's ERS-1 and ENVISAT satellites.

Key words: free-molecular aerodynamics, radiation pressure, non-gravitational perturbations.

## 1. INTRODUCTION

Many space applications require very accurate orbit determinations of a satellite to use position fixes of known precision as absolute reference for high resolution measurements of the geoid, the sea surface topography, or the motions of tectonic plates. With the use of on-board precision tracking aids of ESA's ERS-1 and ERS-2 satellites (laser retro-reflectors LRR, and precise range and range-rate equipments PRARE), and with the use of auxiliary tracking data types (direct altimetry, and altimeter cross-over measurements), the ERS-1 & 2 orbits can be fitted with a root mean square (rms) error of about 5 cm in radial, 10 cm in cross-track, and 40 cm in along-track position. Such precise fits require an orbit prediction software with very accurate models of the perturbing gravitational and non-gravitational accelerations which affect the motion of an Earth satellite. Gravitational perturbations are dominating the force spectrum for most Earth orbits. They are caused by non-uniform mass distributions inside the Earth, by ocean, atmosphere, and Earth tides, and by third body attraction (Sun, Moon, planets). All of these perturbations can be modeled with a high level of confidence, and all of them are conservative (causing only periodic changes in the orbit energy). A complementary class of orbit perturbations is denoted as non-gravitational. This class comprises aerodynamic forces, direct and indirect radiation pressure effects, thermal re-radiation, and charged particle drag. Models of these non-gravitational forces are affected by uncertainties in the molecule-surface and photon-surface interaction processes, in the molecule and photon flux models, and in the solar and geomagnetic activity levels and their effect on the thermosphere and ionosphere. Some of these perturbations cause a secular, time-proportional decrease of the orbital energy, and hence of the orbital altitude. For low-Earth orbits (LEO), these altitude decays must be compensated by periodic maintenance manoeuvres.

A detailed review of non-gravitational forces (also denoted as surface forces) is performed by Rubincam (1982), Klinkrad et al. (1990), and Ries et al. (1992). Apart from the dominant direct and indirect radiation pressure, thermal re-radiation, and aerodynamic perturbations, these papers also analyse secondary effects caused by delayed thermal re-emission due to an Earth shadow transit (Yarkovsky effect), due to the rotation of a satellite (Yarkovsky-Schach effect), or due to a frequency shift between received and emitted radiation (Poynting-Robertson effect). Antreasian & Rosborough (1992) and Powell & Gaposhkin (1988) focus their analysis on radiative forces, including thermal re-radiation, Earth albedo and Earth IR contributions. Aerodynamic forces at LEO altitudes are addressed in more detail by Marcos et al. (1993) and by Koppenwallner et al. (1995). Marcos et al. (1993) and Klinkrad (1996) also investigate the status of contemporary thermospheric models, their uncertainties, and the resulting effects on orbit prediction.

The present paper will describe the nature of surface forces, the key environmental models and their param-

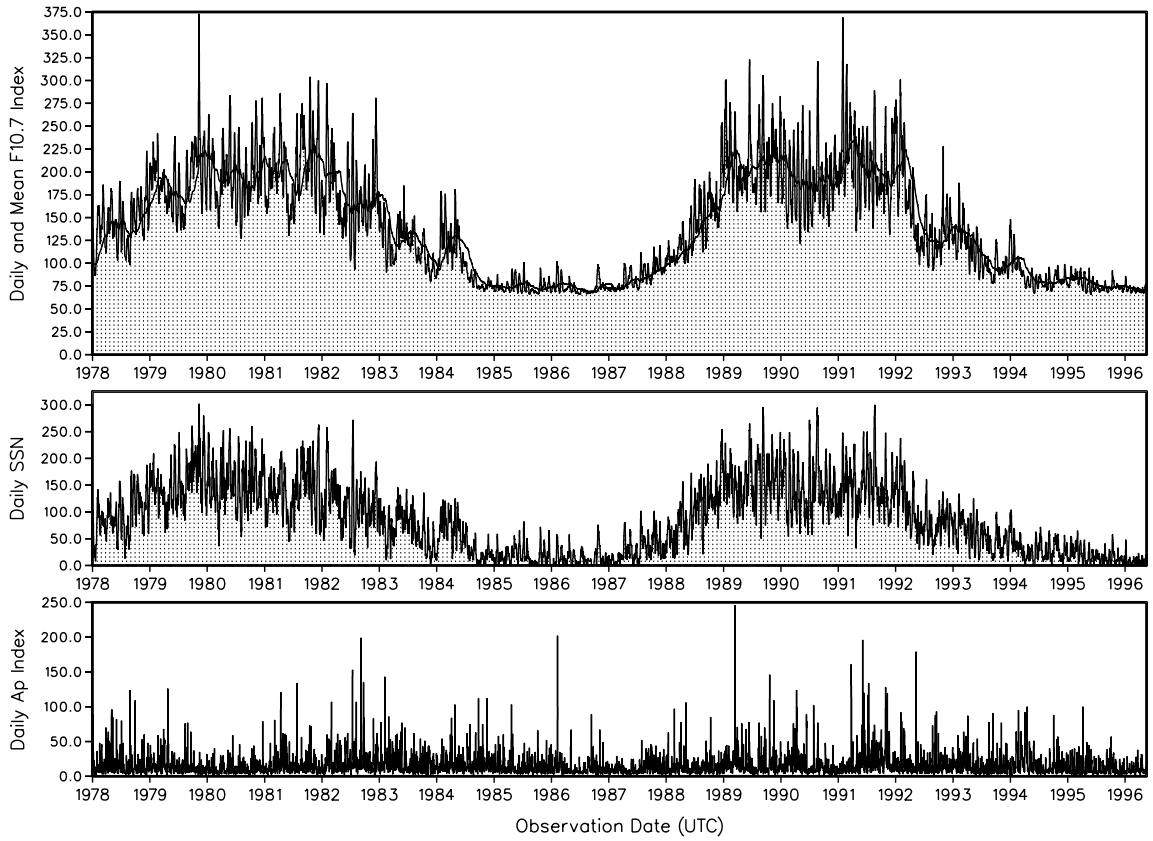


*Figure 1. Observed solar activity (in terms of daily 10.7 cm radio flux $F_{10.7}$, and sun-spot numbers SSN), and geomagnetic activity (in terms of daily $A_p$ indices) during solar cycle 21 and 22.*

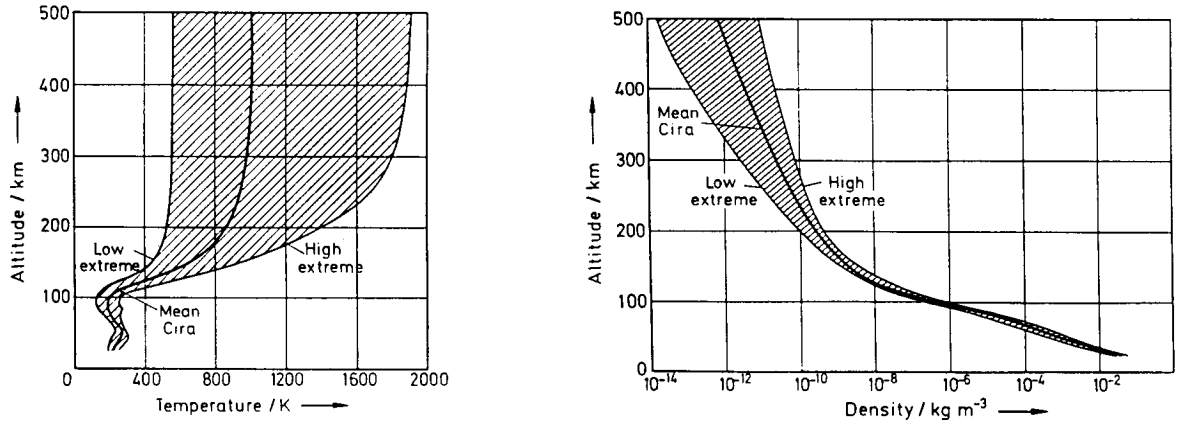


*Figure 2. Temperature and total density altitude profiles and their extremes during a solar cycle according to the CIRA-86 model (equivalent to MSIS-90e at thermospheric altitudes).*

eters, the mathematical methods to determine molecule and photon incident fluxes, the physics of the particle-surface interaction, and the derivation of satellite specific coefficients of force and torque for the different non-gravitational perturbation source terms. Results will be provided for the ERS-1 and ENVISAT satellites, based on runs with ESA's ANGARA program (Analysis of Non-Gravitational Accelerations due to Radiation and Aerodynamics, Fritsche et al. (1998)).

## 2. ENERGY INPUT FROM THE SUN

The only significant energy source for the Earth is the solar radiation which is emitted by the Sun across a wide frequency spectrum with a peak energy flux in the visible light. Its energy distribution can be well approximated by a black body radiator of a mean temperature of 5,785 K, providing a mean energy flux of 1,370 W/m$^2$, with annual

variations of ±3.3% due to the small eccentricity of the Earth orbit. When the energy input into the illuminated hemisphere is averaged over the whole Earth surface, the mean incident energy flux is 349 W/m$^2$, of which 33% is reflected in the visible light as planetary albedo (26% reflected by the clouds, and 7% reflected from the continents and oceans). 67% of the incident energy is absorbed by the atmosphere, by soil, and by water. It is then re-emitted mainly as delayed infra-red (IR) radiation which lets the Earth appear as a black body radiator of a mean temperature of 253 K.

The Sun's input into the terrestrial energy balance drives both aerodynamic and indirect radiation pressure effects (albedo and IR).

## 3. AERODYNAMIC PERTURBATIONS

For LEO satellites, aerodynamic perturbations are mostly of second order. The resulting forces have magnitudes of less than 1/1,000 of the only first order perturbation, the Earth oblateness. Aerodynamic effects (mainly airdrag) are the dominant surface force contributions up to altitudes of 500 km to 600 km (depending on the atmospheric conditions). During re-entries (i.e. below 120 km), aerodynamic forces become first order perturbation quantities which ultimately reach the level of the central attraction term during the atmospheric flight phase. At altitudes above 500 km to 600 km direct solar radiation pressure prevails.

### 3.1. Models of the Earth Atmosphere

While most of the Sun's energy is received in the visible frequency bands, with only minor annual variations, the dynamics of the neutral upper atmosphere is mainly driven by extreme ultra-violet radiation (EUV) and its absorption by atomic oxygen, by photo-dissociation and re-combination processes, and by Joule heating from charged particles which precipitate into the auroral zones. EUV radiation levels are known to change in 11-year solar cycles. They are associated with emissions from Sunspot areas, and are proportional to the observable number of Sun-spots (see Figure 1). The EUV is well correlated with the 10.7 cm solar flux which can be measured on ground through one of the atmospheric radio windows ($F_{10.7}$ is defined in units of $10^{-22} W m^{-2} Hz^{-1}$). Peaks of Joule heating are often associated with high geomagnetic activities. These are commonly measured in terms of daily planetary indices $A_p$, or 3-hourly indices $k_p$ (see Figure 1). Figure 2 shows the effect of low and high extremes of solar and geomagnetic activity on the temperature and air density altitude profile. The temperature profile varies only slightly in the homosphere (below 120 km), and then follows an exponential increase which reaches a limiting value, the so-called exospheric temperature, at the top of the thermosphere. The air density above the turbopause (at 120 km) is determined by the superimposition of concentration profiles $n_i(h)$ of the major atmospheric constituents $N_2$, $O$, $He$, $H$, $O_2$, $Ar$, and $N$ (for $i = 1$ to 7). The concentration scale heights $H_{n_i}$, which determine the decrease in number densities with altitude, are proportional to $M_i/T$, where $M_i$ are the molecular masses of the constituents, and $T$ is the ambient temperature. Hence, the heavy species $N_2$ and $O$ tend

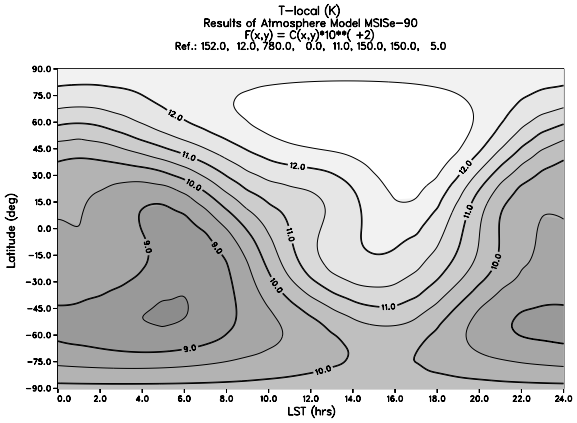


*Figure 3. Diurnal variations of local temperature T according to the MSIS-90e model (level line units:* $100 K$*; conditions: summer solstice, 780 km altitude, mean activities).*

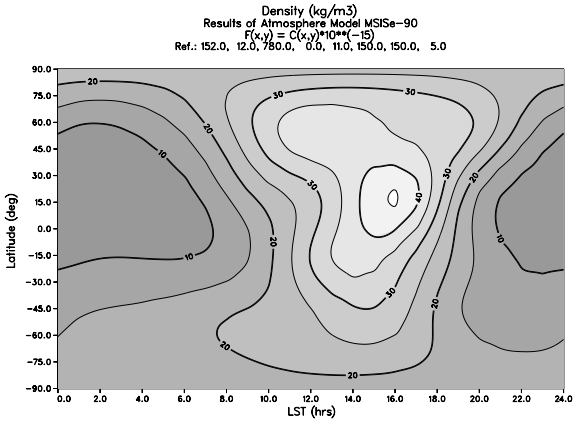


*Figure 4. Diurnal variations of total density* ρ *according to the MSIS-90e model (level line units:* $10^{-15} kg/m^3$*; conditions: summer solstice, 780 km altitude, mean activities).*

to dominate in the lower and middle thermosphere, while the lighter species *He* and *H* prevail in the upper thermosphere and in the exosphere. The altitude region in which $N_2$, $O$, $He$, and finally $H$ dominates is shifted downwards with deceasing temperature (e.g. decreasing activity levels).

Apart from changes with altitude, thermospheric temperatures, concentrations, total densities, and derived quantities (e.g. free mean path lengths) are known to vary with local solar time $t_{lst}$, geographic longitude λ, geodetic latitude ϕ, day of the year $t_d$, mean solar flux $\bar{F}_{10.7}$ (averaged over 81 days = 3 solar rotations), actual solar flux $F_{10.7}$, and current geomagnetic activity $A_p$. The diurnal (day/night) variation profiles of $T$, ρ, $n_O$, and $n_{He}$ are shown in Figures 3 to 6 for at the orbit altitude of ERS-1 and 2. The temperature peak and the peak of the dominant atomic oxygen concentration closely follow the sub-solar point (which is at $t_{lst} = 12$ hrs) with a delay of 3 to 4 hours. The concentration peak of the light weight species helium, however, is closer to the anti-solar point, as a consequence of thermal diffusion. The so-called helium bulge on the winter hemisphere is clearly visible.

The thermosphere described by the MSISe-90 model

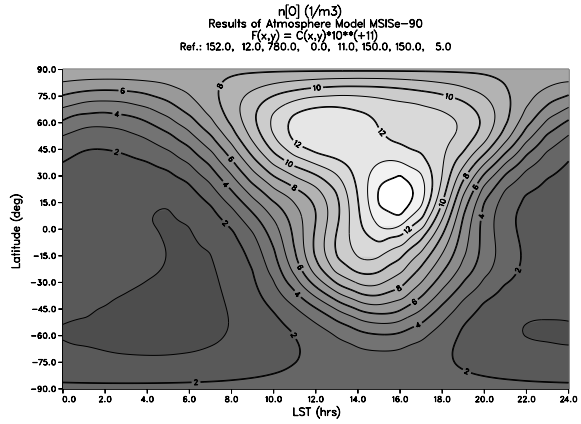


*Figure 5. Diurnal variations of atomic oxygen concentrations according to the MSIS-90e model (level line units: $10^{+11}\,1/m^3$; conditions: summer solstice, 780 km altitude, mean activities).*

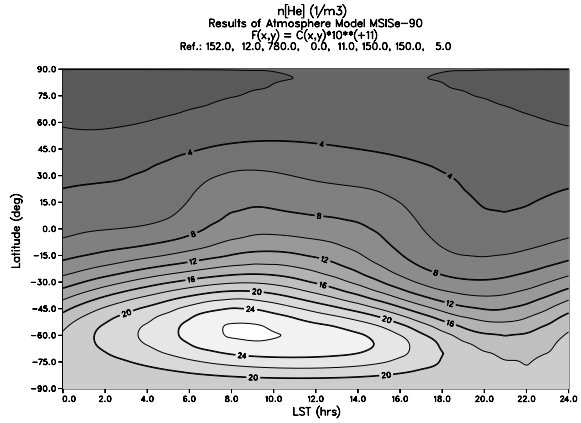


*Figure 6. Diurnal variations of atomic helium concentrations according to the MSIS-90e model (level line units: $10^{+11}\,1/m^3$; conditions: summer solstice, 780 km altitude, mean activities).*

(Hedin (1987) and Hedin (1991a)) is based on the assumption of mass transport by diffusion processes in equilibrium conditions. According to Hedin (1991b), however, there are also thermospheric winds, with directions almost exclusively in the horizontal plane, and with velocities reaching 500 m/s and more. These wind patterns are closely linked with the day/night terminator, with largest magnitudes in polar regions towards the night hemisphere. Due to the increase of viscosity with altitude, the magnitude of these winds reduces towards the thermopause.

### 3.2. Aerodynamic Coefficients of a Satellite

For a spacecraft which moves through the upper atmosphere with a relative velocity of $U_\infty$ and a mean cross-section of $A_{ref}$, the encountered aerodynamic force $\vec{F}_a$ can be computed by a summation of individual contributions from all of the 7 atmospheric constituents ($i = 1$ to 7 for $N_2$, $O$, $He$, $H$, $O_2$, $Ar$, and $N$), with partial densities $\rho_i$.

$$\vec{F}_a = \sum_{i=1}^{7} \frac{1}{2}\rho_i A_{ref} U_\infty^2 \vec{C}_{a_i} \tag{1}$$

In this equation, all aerodynamic force characteristics are concentrated in $\vec{C}_{a_i}$, which is a function of the spacecraft geometry, its surface properties, and its attitude relative to the air flow. If one assumes that a fraction $\sigma_d$ (where $0 \le \sigma_d \le 1$) of the incoming molecules is diffusely reflected according to a Lambert distribution, and that the complement is specularly reflected, then the local contribution to $\vec{C}_{a_i}$ can be described analytically.

$$\vec{C}_{a_i} = \frac{1}{A_{ref}} \int_{(A)} \left(\sigma_d\, \vec{c}_{i,d}(\vec{r}) + (1-\sigma_d)\, \vec{c}_{i,s}(\vec{r})\right) dA \tag{2}$$

The vector quantities $\vec{c}_{i,d}(S_{\infty_i}, T_w/T_\infty)$ and $\vec{c}_{i,s}(S_{\infty_i})$ are the diffuse and specular reflection coefficients for a surface element $dA$ at the position $\vec{r}$ on that part of the spacecraft surface $A$ which is exposed to the airflow. $\vec{c}_{i,d}$ has components normal and tangential to the surface element (along $\vec{n}$ and $\vec{t}$), where the normal (= pressure) contribution is also depending on the wall temperature $T_w$. $\vec{c}_{i,s}$ only contributes to the local normal force.

$$\begin{aligned} \vec{c}_{i,d} &= \left(\frac{1}{\sqrt{\pi}}\frac{\Pi(S_{n_i})}{S_{\infty_i}^2} + \frac{1}{2}\sqrt{\frac{T_w}{T_\infty}}\frac{\chi(S_{n_i})}{S_{\infty_i}^2}\right)\vec{n} \\ &+ \left(\frac{1}{\sqrt{\pi}}\frac{S_{t_i}\,\chi(S_{n_i})}{S_{\infty_i}^2}\right)\vec{t} \end{aligned} \tag{3}$$

$$\vec{c}_{i,s} = \frac{2}{\sqrt{\pi}}\frac{\Pi(S_{n_i})}{S_{\infty_i}^2}\,\vec{n} \tag{4}$$

The auxiliary quantities $\Pi(S_{n_i})$ and $\chi(S_{n_i})$ are defined as

$$\Pi(S_{n_i}) = S_{n_i}\exp\left(-S_{n_i}^2\right) + \sqrt{\pi}\left(S_{n_i}^2 + \frac{1}{2}\right)\left(1+\mathrm{erf}(S_{n_i})\right)$$

$$\chi(S_{n_i}) = \exp\left(-S_{n_i}^2\right) + \sqrt{\pi}S_{n_i}\left(1+\mathrm{erf}(S_{n_i})\right)$$

Here, $S_{\infty_i} = \sqrt{M_i U_\infty^2/2kT_\infty}$ is the molecular speed ratio (free stream velocity $U_\infty$ divided by the most probable thermal velocity of the $i$-th atmospheric species), $M_i$ is the molar mass of a contributing gas species, $T_\infty$ is the ambient temperature, and $k$ is the Boltzmann constant. $S_{n_i}$ and $S_{t_i}$ are the normal and tangential components of $S_{\infty_i}$ for a particular element of the exposed spacecraft surface $A$, over which the forces are integrated.

The ANGARA program (Fritsche et al. (1998)) uses the outlined method to compute aerodynamic coefficients of force and torque in an analytical way (so-called Integral Method). Alternatively, a numerical Monte-Carlo Test-Particle (MCTP) Method is implemented. Both methods consider geometric shadowing in their analysis, but the MCTP also considers multiple reflections, and an alternative, more detailed surface interaction model according to Schaaf and Chambre.

## 4. RADIATION PRESSURE PERTURBATIONS

Radiation pressure is the dominant non-gravitational perturbation at satellite altitudes above 500 km to 600 km

(depending on solar activity). In order of significance, there are four major radiation sources: the direct radiation from the Sun, the albedo re-radiation reflected from the illuminated Earth hemisphere, the more uniformly re-emitted Earth IR radiation, and directed IR radiation emitted from the spacecraft (denoted as thermal thrust). The sources of these contributions, and the computation of their perturbation forces will be addressed hereafter.

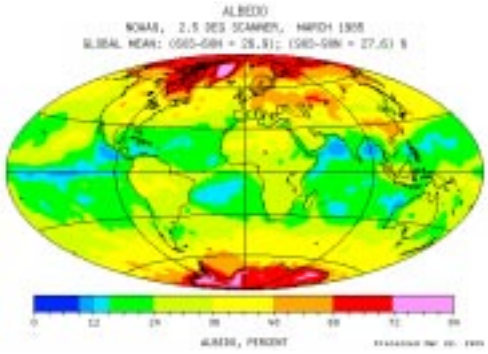

*Figure 7. Planetary albedo map composed from NOAA-9 data (based on observations in March 1985).*

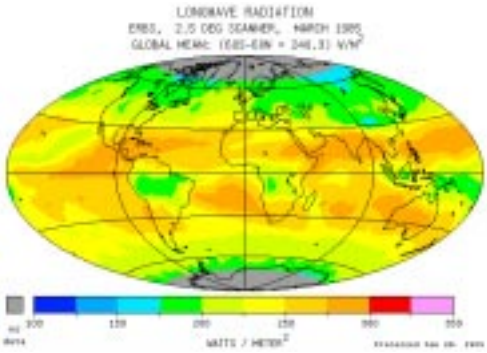

*Figure 8. Earth IR re-radiation map composed from ERBE data (based on observations in March 1985).*

### 4.1. Models of Radiation Sources

The solar energy flux has a spectral distribution which closely follows Planck's law for a black body radiator of a mean temperature of $T = T_{\odot} = 5,785K$. The peak of the energy flux (described by Wien's formula) is reached in the visible light. Integrating the Sun's radiation spectrum over all frequencies, leads to an energy flux of $\dot{e}(r_{\odot}) = \dot{e}_{\odot}$ on the Sun's surface according to the Stefan-Boltzmann law

$$\dot{e} = \sigma T^4 \tag{5}$$

where $\sigma = 5.67 \times 10^{-8} W m^{-2} K^{-4}$).

The initial energy flux of $\dot{e}(r_{\odot}) = \dot{e}_{\odot} = 6.4 \times 10^7 W/m^2$ is reduced to a mean value of $\dot{e}(r_{\oplus}) = 1370 W/m^2$ at the distance $r_{\oplus}$ of the Earth, with annual variations of $\pm 3.3\%$ due to the eccentricity of the Earth orbit. About 33 % of the incident energy is reflected in the visible light spectrum from the top of the cloud cover, from the atmosphere, and from the Earth surface. Figure 7 shows the resulting planetary albedo distribution of the Earth for March 1985 (NOAA-9 data, NASA (1996)). The largest albedos are observed in polar regions, due to the snow and ice cover, while equatorial albedos are generally smaller. Re-radiation from the Earth albedo is only effective for those parts of the surface and atmosphere which are located in the Sun-illuminated hemisphere.

Another secondary source of re-radiation is the time-delayed and frequency shifted re-emission in the IR wavelengths of 67 % of the solar energy flux which is absorbed by the Earth atmosphere, the continents, and the oceans. Figure 8 shows the global distribution of the terrestrial IR energy flux as observed by the ERBE satellite (Earth Radiation Budget Experiment, NASA (1996)) in March 1985. This re-radiation is almost independent of the illumination conditions, with a mean level of $\dot{e}_{\oplus} = 234 W/m^2$, corresponding to a black body radiator with a temperature of $T_{\oplus} = 253K$.

When viewed from a mean heliocentric Earth distance of $1.5 \times 10^6$ km (1 astronomical unit), the Sun covers a solid angle of about $0.5°$. This light source of finite extension causes a core shadow (umbra), and a semi shadow region (pen-umbra) on satellite orbits which pass through eclipse. The edges of the core shadow region also receive radiation due to atmospheric refraction, which can cause deflections of solar rays by up to $1.3°$, increasing the geometrically defined semi-shadow region (with a cone angle of about $0.5°$) by up to a factor 7.

Satellites do not only receive and reflect direct solar radiation, but they also heat up due to external and internal energy inputs. A non-uniform re-emission of this energy over the spacecraft surface (e.g. due to shadowing) can cause a non-zero force (Antreasian & Rosborough (1992) and Powell & Gaposhkin (1988)). Such an effect has been observed for the GPS satellites due to thermal energy emission from their radiator panels.

### 4.2. Radiation Coefficients of a Satellite

The radiation energy flux $\dot{e}$ which is intercepted by a satellite at a certain frequency $\nu$ corresponds to a photon impingement rate of

$$\dot{n}_p = \dot{e}/(h\nu) \tag{6}$$

where $h = 6.625 \times 10^{-34} Js$ is Planck's constant. Of the incoming photons, a fraction $\alpha$ is absorbed , a fraction $\rho_s$ is specularly reflected, and a fraction $\rho_d$ is diffusely reflected according to a Lambert distribution (cosine law). If one assumes a non-transparent surface, the energy conservation can be expressed as

$$\alpha + \rho_s + \rho_d = 1 \tag{7}$$

All of these coefficients normally depend on the surface material, its temperature, and the wavelength and incident angle of the photons. Together with the emissivity $\varepsilon$, which describes the IR re-radiation properties, this set of parameters completely defines the photon-surface interaction. The ratio of $\alpha/\varepsilon$ can vary over a wide range (e.g. 0.98/0.98 for black paint, 0.79/0.81 for solar cells, 0.45/0.80 for aluminized Kapton, and 0.07/0.76 for silver Teflon).

If one assumes radiation point sources at an infinite distance from the satellite, then the resulting radiation force

$\vec{F}_r$ can be described as

$$\vec{F}_r = \sum_{n=1}^{4} \frac{\dot{e}_n}{c} A_{ref} \vec{C}_{r_n} \tag{8}$$

where $n = 1$ to 4 represents direct, Earth albedo, Earth IR, and thermal radiation, $\dot{e}_n$ is the energy flux at the respective wavelength, $c$ is the speed of light, and $A_{ref}$ is a spacecraft reference cross-section. The radiation force coefficients $\vec{C}_{r_n}$ for the different radiation sources can be determined by integration over the illuminated surface $A_n$ of the satellite (which is different for each radiation source).

$$\vec{C}_{r_n} = \frac{1}{A_{ref}} \int_{(A_n)} \vec{c}_{r_n}(\vec{r})\, dA \tag{9}$$

The local contributions $\vec{c}_{r_n}(\vec{r})$ from a surface element $dA$ at its location $\vec{r}$ are defined by the unit vectors of the incident direction $\vec{u}_n$ relative to the surface normal $\vec{n}$, and by the frequency dependent reflection properties (where $\alpha_n$ was expressed in terms of $\rho_{s_n}$ and $\rho_{d_n}$ via equation 7).

$$\begin{aligned} \vec{c}_{r_n}(\vec{r}) &= (\vec{u}_n\vec{n})\,(1-\rho_{s_n})\,\vec{u}_n + \frac{2}{3}\frac{\sigma}{c}\varepsilon_n T_w^4\,\vec{n} \\ &+ (\vec{u}_n\vec{n})\left(2\rho_{s_n}\,(\vec{u}_n\vec{n}) - \frac{2}{3}\rho_{d_n}\right)\vec{n} \end{aligned} \tag{10}$$

For software implementation purposes, the radiation coefficients $\vec{C}_{r_n}$ are computed separately for each of the four major sources. For each source, a single, most probable frequency is adopted, and non-uniform radiation input distributions (i.e. Earth IR and Earth albedo) are discretised into a finite number of planar sources, with each of them emitting parallel beams towards the spacecraft, while observing spacecraft-to-ground visibility constraints (and ground illumination conditions in case of albedo). For direct solar radiation and spacecraft thermal radiation the umbra and pen-umbra eclipse conditions are considered, including refraction and absorption of visible light by the Earth atmosphere.

Similar to the aerodynamic analysis, the ANGARA program (Fritsche et al. (1998)) determines spacecraft specific coefficients of force and torque for each radiation effect by using either an analytical Integral Method, or a numerical Monte-Carlo Test-Particle Method (MCTP). As before, both methods consider geometric shadowing, but the MCTP method also allows multiple reflections (which can be important for torques).

## 5. DISCUSSION OF RESULTS

Non-gravitational perturbation forces (also denoted as surface forces) can play an important role in satellite operations. For the dominant class of low-Earth orbiting objects (which account for about 85% of all tracked objects) it is mainly the airdrag which due to its energy dissipation affects orbit decay rates, and hence orbit maintenance frequencies in case of controlled satellites (e.g. ERS-1 & 2). At higher orbit altitudes, and in case of highly eccentric orbits (e.g. ISO), solar radiation pressure becomes the dominant surface force which affects orbit and attitude maintenance cycles.

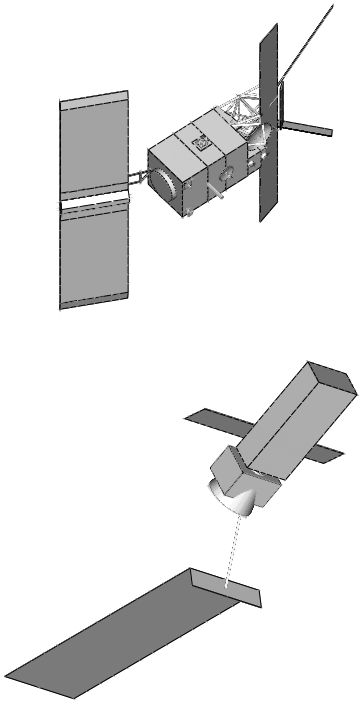

*Figure 9. Geometric models of the ERS-1 satellite (top), and of the ENVISAT satellite (bottom), as generated and used by the ANGARA program (displayed in different scales).*

### 5.1. Effects of Surface Forces

Abandoned LEO objects ultimately re-enter into the denser layers of the Earth atmosphere, where they mostly burn up. Statistically, one object of a radar cross-section (RCS) larger than 1 m$^2$ decays each week. Occasionally, such uncontrolled re-entries involve spacecraft with large masses (e.g. 75 t for Skylab-1 and 40 t for Salyut-7), or hazardous payloads (e.g. nuclear reactors on Kosmos-954 and 1402), parts of which can reach the ground. During the re-entry prediction campaigns for these high risk objects, the strong effects of solar and geomagnetic activity fluctuations could be observed (see Figure 1):

- 11-Jul-1979: Skylab-1 re-enters over the Indian Ocean and Australia at the start of the maximum of solar cycle 21. Intensive studies of the aerodynamic behavior allow a forward shift of the impact footprint by inducing a tumble 8 hours before the entry.
- 07-Feb-1983: The detached reactor of Kosmos-1402 re-enters over the South Atlantic, 15 minutes before reaching Europe. The high level of airdrag at the end of the maximum of solar cycle 21 is further enhanced by a geomagnetic storm of magnitude $A_p = 150$ on Feb. 5. The remaining lifetime was hereby shortened by 30%.
- 07-Feb-1991: Salyut-7 (with Kosmos-1686 attached) re-enters over South America. The orbit lifetime was strongly reduced by the peak of solar cycle 22 ($F_{10.7} = 369$ on Jan. 30).

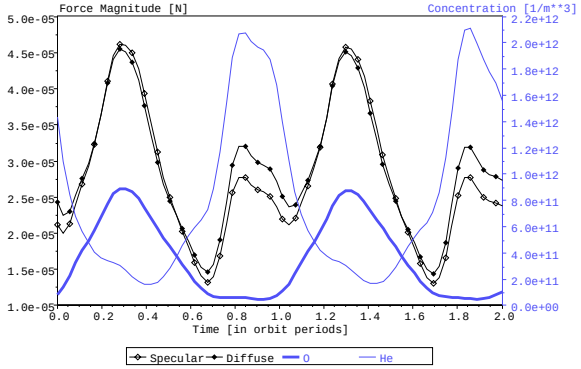


*Figure 10. Aerodynamic force magnitude for ENVISAT over 2 orbits, for specular and diffuse reflection laws, as a function of the local atmosphere composition.*

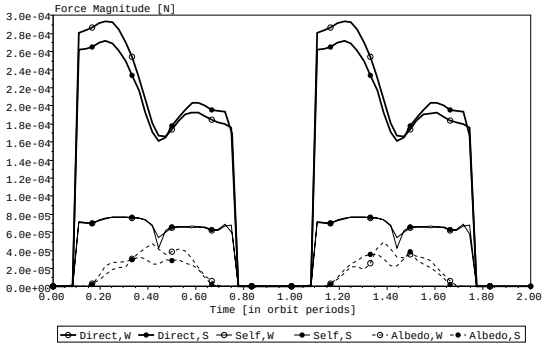


*Figure 12. Direct radiation and thermal radiation force magnitude for ERS-1 over 2 orbits, for winter and summer solstice conditions.*

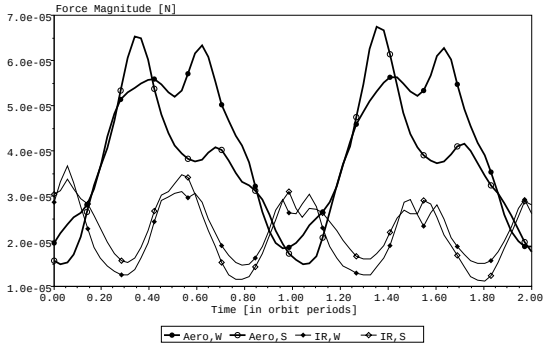


*Figure 11. Aerodynamic and Earth IR force magnitude for ERS-1 over 2 orbits, for winter and summer solstice conditions.*

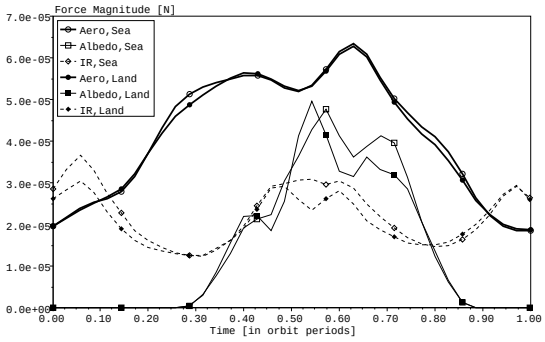


*Figure 13. Aerodynamic, Earth albedo, and Earth IR force magnitude for ERS-1 over one orbit, for a 'sea' and 'land' groundtrack.*

In routine operations the orbit decay of LEO satellites is periodically adjusted to maintain the orbit altitude. The frequency of necessary orbit manoeuvres is depending on the allowed offsets in altitude and groundtrack pattern (for ERS-1 & 2 the groundtrack must be maintained to within $\pm 1$ km), and it is also determined by the required periods of undisturbed payload operation. Surface forces also play an important role in precise orbit determination of satellite programs such as GPS (Powell & Gaposhkin (1988)), LAGEOS (Rubincam (1982)), TOPEX-POSEIDON (Antreasian & Rosborough (1992)), and ESA's ERS-1, ERS-2 and ENVISAT spacecraft, where in some cases radial orbit accuracies of a few centimeters are required.

## 5.2. Aerodynamic Forces on ERS-1 and ENVISAT

ESA's operational ERS-1 and ERS-2 satellites, and the planned ENVISAT mission are using near-circular orbits ($e = 0.001$) of retro-grade inclinations ($i = 98.52°$) at altitudes near 780 km. For the selected altitude and inclination the orbit planes are rotating Sun-synchronously at a rate of $0.986°/\text{day}$ under the influence of the Earth oblateness. The descending orbit nodes are thus kept at 10:30 mean local solar time. The satellites are maintained in an attitude of local normal pointing along the geodetic vertical (roll and pitch control), with a yaw steering such that the cross-track radar beams are pointing along the zero Doppler line. The ERS-1 & 2 altitude decay can range from 0.5 m/d to 10 m/d between very low and extremely high solar activity.

The ANGARA program was used to perform a full aerodynamic analysis (forces and torques) for ERS-1 and ENVISAT. The corresponding surface geometry models, which consist of 11,376 and 7,644 panels, respectively, are shown in Figure 9. For the analysis, two orbits were predicted with the relevant attitude steering profiles superimposed. In Figure 10 the importance of gas-surface interaction processes is highlighted for ENVISAT. The marked curves show the aerodynamic force magnitude (left axis) in case of perfectly diffuse ($\sigma_d = 1$, filled diamond), and in case of perfectly specular reflection ($\sigma_d = 0$, hollow diamond). The force history is correlated with the changing dominance of the prevailing atmospheric constituents *He* and *O* (right axis), with stronger specular reflections from atomic oxygen, and a tendency towards diffuse re-emission from helium. This is related to the species dependent molecular speed ratio $S_{\infty_i} \propto \sqrt{M_i}$ (with $M_i = 4$ for *He* and 16 for *O*) and its effect on equations 3 and 4. In Figure 11 the sensitivity of aerodynamic perturbations with seasonal changes of the upper atmosphere is analysed for ERS-1 at the time of summer solstice (hollow circle) and winter solstice (filled circle). The signature of the diurnal density bulge, which moves with the sub-solar point, is clearly visible, generating seasonal differences in the aerodynamic drag level of up to 30% at the same orbit locations (see also Figure 4).

### 5.3. Radiation Forces on ERS-1

The altitude $h_{r\geq a}$ beyond which radiation perturbations are dominating over aerodynamic forces can be determined from equations 1 and 8 to be

$$h_{r\geq a} = h_o - H_{\rho_o} \ln\left(\frac{2\dot{e}(r_\oplus)}{c\rho_o U_\infty^2}\right) \qquad (11)$$

where $h_o$ is a reference altitude (e.g. 400 km) at which the mean air density $\rho_o$ and the corresponding density scale height $H_{\rho_o}$ are defined. Between low and high extremes of solar activity the mean air density at 400 km increases by a factor of about 10, from $10^{-12}$ to $10^{-11}$ kg/m$^3$, leading to low and high extremes of $h_{r\geq a}$ between 500 and 600 km.

In Figures 11 and 12 the radiation perturbation magnitudes due to direct solar radiation, Earth IR and Earth albedo re-radiation, and thermal radiation from the spacecraft are plotted over two orbits of ERS-1 at summer solstice and winter solstice conditions. A comparison with concurrent aerodynamic forces in Figure 11 shows that direct radiation pressure generates perturbation amplitudes which are more than 4 times larger than those from airdrag at mean solar activity levels. The seasonal differences in the radiation force magnitudes are less than 10% and can be attributed to annual changes in the Sun-Earth distance (for direct radiation), and to annual changes in albedo and IR re-radiation characteristics of the Earth (for indirect radiation). The thermal radiation emission by the spacecraft itself is almost unaffected by seasonal changes, except for shifts of the 33 minutes eclipse mask near the ascending node. This Earth shadow transit also affects the direct solar radiation with an almost instantaneous on/off switching, which is only damped by pen-umbra and atmospheric refraction effects. Likewise, the albedo re-radiation is deactivated while the night hemisphere of the Earth comes into the field of view of the satellite (which is a more gradual process).

The Earth albedo and Earth IR perturbations are related to underlying re-radiation maps in a geographic longitude/latitude coordinate system (see Figure 7 and 8). The effect of the longitude position of the ascending node of an ERS-1 orbit on the albedo and IR force profiles is analysed in Figure 13 for a groundtrack with a large land and sea coverage, respectively (airdrag profiles are included as reference). The maximum difference in albedo and IR perturbation force amplitudes due to groundtrack coverage is on the order of 10%.

## 6. CONCLUSIONS

Good models of non-gravitational perturbations are a prerequisite in precise orbit determination applications, predominantly for navigational constellations (e.g. GPS and GLONASS) and satellite programs with geodetic mission objectives (e.g. LAGEOS, ERS-1 & 2, and TOPEX-POSEIDON). The dominant surface forces which need to be modeled are due to direct radiation (from the Sun), indirect radiation (from Earth albedo and IR), and spacecraft emitted thermal radiation. Aerodynamic perturbations are only important for LEO satellites and start to be dominating below 500 to 600 km (depending on solar activity).

The resulting forces and torques due to photon and molecule impingement on the spacecraft surface (hence the term "surface forces") can be modeled by means of semi-analytical integral methods or numerical Monte-Carlo test-particle methods for spacecraft geometries and surface models of arbitrarily high resolution and fidelity. Computerised non-gravitational force models (e.g. ESA's ANGARA program, Fritsche et al. (1998)), are mainly limited by intrinsic inaccuracies of the environment descriptions (e.g. atmosphere, Earth albedo and IR distribution), and by the limited knowledge on the surface interaction parameters of photons and molecules as a function of the surface material and incident particle properties. Supporting experimental data in this area will be required to further improve theoretical models of non-gravitational effects.

## REFERENCES


Antreasian, P.G., and Rosborough, G.W., *Prediction of Radiant Energy Forces on the TOPEX/POSEIDON Spacecraft*, AIAA Journal of Spacecraft and Rockets, vol. 29, no.1, pp. 81–90, Jan/Feb, 1992

Fritsche, B., Ivanov, M., Kashkovsky, A., Koppenwallner, G., Kudrayavtsev, A., and Zhukova, G., *Radiation Pressure Forces on Complex Spacecraft*, final report, ESA contract no. 11908/96/D/IM, 1998

Hedin, A.E., *MSIS-86 Thermospheric Model*, Journal of Geophysical Research, vol. 92, no. A5, pp. 4649–4662, 1987

Hedin, A.E., *Extension of the MSIS Thermosphere Model into the Lower Atmosphere*, Journal of Geophys. Res., vol. 96, no. A2, pp. 1159–1172, 1991

Hedin, A.E., Biondi, M.A., Burnside, R.G., Hernandez, G., Johnson, R.M., Killeen, T.L., Mazaudier, C., Meriwether, J.W., Salah, J.E., Sica, R.J., Smith, R.W., Spencer, N.W., Wickwar, V.B., and Virdi, T.S., *Revised Model of the Thermosphere Winds Using Satellite and Ground-based Observations*, Journal of Geophys. Res., vol. 96, no. A5, pp. 7657–7688, 1991

Klinkrad, H., Koeck, C., and Renard, P., *Precise Satellite Skin-Force Modeling by Means of Monte-Carlo Ray-Tracing*, ESA Journal, vol. 14, pp. 409–430, 1990

Klinkrad, H., *On the Use of Atmosphere Models in Re-Entry Predictions*, ESA SP-392, pp. 287–298, 1996

Koppenwallner, G., Johansmeier, D., Klinkrad, H., and Ivanov M., *A Rarefied Aerodynamics Modeling System for Earth Satellites (RAMSES)*, Rarefied Gas Dynamics, vol. 19, Oxford Science Publications, pp. 1366–1372, 1995

Marcos, F.A., Baker, C.R., Bass, J.N., Killeen, T.L., and Roble, R.G., *Satellite Drag Models: Current Status and Prospects*, AAS/AIAA Astrodynamics Specialist Conference, Victoria/B.C., Aug. 16–19, 1993

NASA Langley Research Center, *ERBE Monthly Scanner Data Products*, CD ROM distributed by the NASA Distributed Active Archive Center, 1996

Powell, G.E., and Gaposhkin, E.M., *Modeling of Non-Gravitational Effects on GPS Satellites*, AIAA paper no. 88-4291-CP, 1988

Ries, J.C., Shum, C.K., and Tapley, B.D., *Surface Force Modeling for Precision Orbit Determination*, IUGG General Assembly, Symp. U15, 1992

Rubincam, D.P., *On the Secular Decrease in the Semimajor Axis of LAGEOS's Orbit*, Celestial Mechanics, vol. 26, pp. 361–382, 1982